Probing a dusty magnetized plasma with self-excited dust-density waves

Benjamin Tadsen,* Franko Greiner, and Alexander Piel
IEAP, Christian-Albrechts-Universität, 24098 Kiel, Germany

(Received 30 November 2017; published 14 March 2018)

A cloud of nanodust particles is created in a reactive argon-acetylene plasma. It is then transformed into a dusty magnetized argon plasma. Plasma parameters are obtained with the dust-density wave diagnostic introduced by Tadsen *et al.* [Phys. Plasmas **22**, 113701 (2015)]. A change from an open to a cylindrically enclosed nanodust cloud, which was observed earlier, can now be explained by a stronger electric confinement if a vertical magnetic field is present. Using two-dimensional extinction measurements and the inverse Abel transform to determine the dust density, a redistribution of the dust with increasing magnetic induction is found. The dust-density profile changes from being peaked around the central void to being peaked at an outer torus ring resulting in a hollow profile. As the plasma parameters cannot explain this behavior, we propose a rotation of the nanodust cloud in the magnetized plasma as the origin of the modified profile.

DOI: 10.1103/PhysRevE.97.033203

I. INTRODUCTION

Magnetized complex plasmas have gained much attention in the past two decades [1–3]. This is attributed to the finding and investigation of dust clouds in space [4] and in fusion devices [5,6] where magnetic fields are present. From the theoretical point of view, magnetized dusty plasmas are of interest because charging, transport, and diffusion in a magnetized system are fundamentally different from the unmagnetized situation [7–10].

A magnetic field has a strong influence on the wake of a micrometer-sized dust particle in a flowing plasma [11,12]. Also, magnetized systems show modified properties in their modes [13] and waves [14].

For the setup of a magnetized dusty plasma experiment there have been many different approaches employing permanent [15], water-cooled copper-coil [16], and superconducting magnets [17]. Both dc and rf discharges are in use. Since a setup with a high induction cannot be installed on an airplane or the International Space Station, these experiments are ground based and mainly limited to two-dimensional (2D) systems.

The combination of a magnetic field with gravity on Earth makes such experiments difficult as dust particles larger than a micron only populate the lower sheath, resulting in a dust-free plasma in the bulk. Additionally, magnetized plasmas tend to filamentation [18,19], which creates a disturbed plasma environment for the dust. Therefore, we have carried out experiments with nanodust particles. They fill the whole plasma volume except for a small void in the center. As long as the plasma is sufficiently filled with particles, the filamentation is suppressed [20].

We examined the inner cloud structure by taking extinction images and measuring the polarization state of scattered light from the dust particles. This allows us to determine the size and density of the dust particles in the magnetized plasma. Plasma parameters and the electric-field strength inside the dust cloud are deduced from the properties of dust-density waves (DDWs) [21]. From these diagnostics we aim to determine and explain the cloud shape in the unmagnetized and the magnetized situation.

II. EXPERIMENTAL SETUP

A. Basic components

The plasma chamber, rf circuit, and grounding are described in Ref. [20]. A side view sketch of the experiment is shown in Fig. 1. Here we used shielded electrodes with a diameter of 50 mm and a vertical gap of 32 mm. The working gas is argon at a pressure of 4 Pa. The plasma is generated with an rf source in symmetric push-pull mode with an rf power of 10 W at 13.56 MHz. The electrode shield and the plasma chamber are grounded. Neutral gas flows from top to bottom through the chamber. We use an admixture of 20% acetylene (C_2H_2) to the argon gas to grow nanoparticles in the resulting reactive plasma. The acetylene flow is shut off when the dust particles have reached the appropriate size. In the configuration used particles are monodisperse and spherical [22,23].

The dust is monitored using several optical diagnostics around the chamber as shown in Fig. 2. For the determination of the particle size, a laser is sent through the dust cloud, which is polarized with an angle of 45° with respect to the scattering plane (laser 2). The polarization state of the scattered light is measured using a commercial rotating compensator ellipsometer, which allows one to determine the refractive index and the time-resolved size information using the CRAS-Mie algorithm (Constant Refractive index - Arbitrary Size using Mie theory, see Ref. [23]). This is illustrated in Fig. 3 and Table I.

To gain a complete image of the confinement situation, a reliable 2D method for measuring the dust density is needed. Since the dust cloud has cylindrical symmetry [25], we perform a simultaneous 2D extinction measurement and calculate the actual dust-density distribution from it by applying the inverse

*tadsen@physik.uni-kiel.de

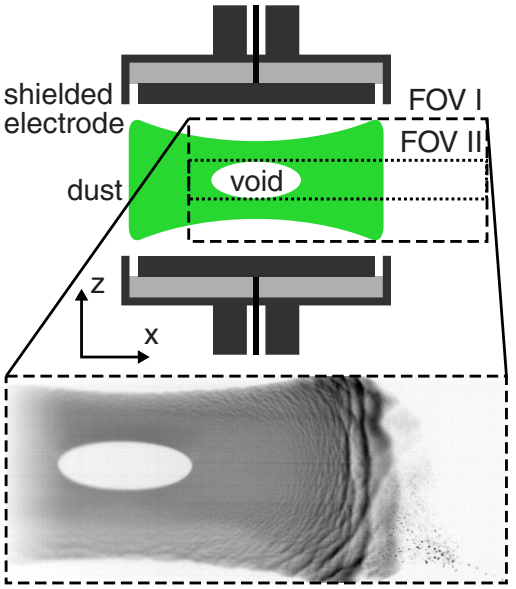

FIG. 1. Side view sketch of the experiment with field of view accessible by the DDW camera to cover the whole cloud (FOV I) or for a central stripe (FOV II) to record a video at a high frame rate.

Abel transform [26]. For this purpose, a green LED panel as a light source and a camera with a telecentric lens are mounted to measure the optical depth τ of the dust cloud.

Finally, we use a camera to capture the DDWs propagating in a central vertical plane, which is illuminated using a green laser sheet (laser 1). Depending on the chosen size of the field of view (FOV, see Fig. 1), the recorded videos have a maximum frame rate of 2 kHz.

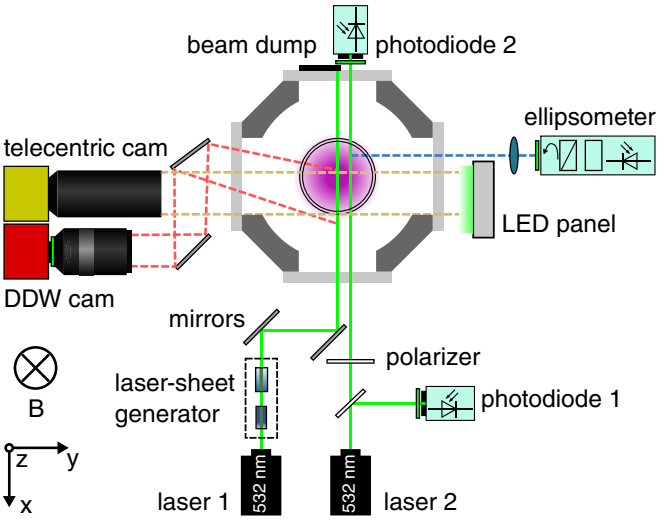

FIG. 2. Top view sketch of the optical diagnostics used for the experiment. Electrodes and Faraday shields are shown as two circles in the center. The extent of the plasma is visible in fading violet. Viewing directions of different diagnostics are plotted as dashed lines. The DDW camera, ellipsometer, and photodiodes are shielded against plasma emission with 532-nm interference filters. Since all diagnostics use green light, they can only be used one after another.

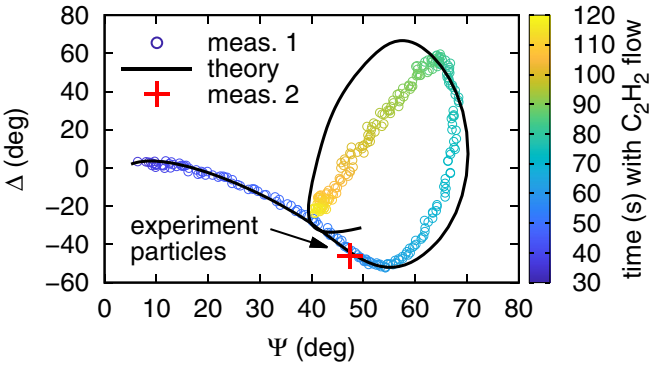

FIG. 3. Ellipsometric angles Ψ and Δ of the scattered light measured during a particle growth process (circles) and theoretical black curve calculated with the CRAS-Mie algorithm [23]. The deviation between theory and experiment during the late growth stage is due to multiple scattering within the dust cloud [24]. A second run of the process is terminated by shutting off the acetylene at $t = 50$ s. Shortly after, Ψ and Δ were measured (red plus). The resulting parameters from measurement 2 are shown in Table I. A detailed description of the procedure is given in Sec. II B.

B. Experiment schedule

In order to confine nanodust particles in a magnetized plasma, a specific procedure is followed. As a preparatory measure the growth process is characterized. To start the growth, the argon working gas gets a 20% admixture of acetylene, totaling to a flow of 8 cm^3/min at STP. During this step, dust particles are formed in the plasma at a pressure of roughly 25 Pa. Their scattering properties are measured and shown as colored circles in Fig. 3. The $\Delta(\Psi)$ curve is analyzed with the CRAS-Mie algorithm [23] providing the refractive index, the time-resolved particle size, and the extinction efficiency.

Repeating the process and shutting off the acetylene flow 50 s after it was initiated allows one to select particles of a certain radius a. The scattering properties of these dust particles are shown by a red plus in Fig. 3. Evaluating the ellipsometric angles at this plus with the aid of the theory curve in black results in the particle data depicted in Table I, mainly the particle radius $a = 150$ nm.

Self-excited waves are more pronounced if their frictional damping is low. Consequently, the neutral pressure is reduced to 4 Pa after nanoparticle creation. The magnetic induction is ramped from 0 to 100 mT within a couple of seconds, providing the environment for a magnetized plasma. Then the DDWs and the density distribution are measured successively at 100,

TABLE I. Results of the CRAS-Mie algorithm for the particles represented by the marked position (+) in Fig. 3. These particles were used for the magnetic-field experiments.

Parameter	Symbol	Value
particle radius	a	152 nm
refractive index	m	$1.74 + 0.07i$
extinction efficiency	Q_{ext}	2.91

50, 20, 10, and 0 mT. The respective data are analyzed and discussed in the following sections.

C. Magnetization

The investigations were performed in the DUSTWHEEL, a water-cooled magnet [16] capable of magnetic inductions up to 400 mT. We used a maximum of 100 mT.

To quantify the influence of the magnetic field, the susceptibility of a plasma species j can be obtained by performing a perturbation analysis in the governing equations, namely, continuity, Poisson, and momentum transfer equations. This yields

$$0 = 1 + \sum_{j=\mathrm{i,e,d}} \frac{\omega_{\mathrm{p}j}^2 \Omega_{1\mathrm{c}j}^2}{k^2 v_{T_j}^2 \Omega_{1\mathrm{c}j}^2 - \Omega_{1j}\Omega_{2j}\Omega_{2\mathrm{c}j}^2}, \tag{1}$$

including the wave frequency ω and wave number k as well as the following abbreviated quantities:

$$\Omega_{1j} = \omega - \vec{k}\cdot\vec{v}_j, \tag{2}$$

$$\Omega_{2j} = \omega - \vec{k}\cdot\vec{v}_j + i\nu_{j\mathrm{n}}, \tag{3}$$

$$\Omega_{1\mathrm{c}j}^2 = \Omega_{2j}^2 - \omega_{\mathrm{c}j}^2 \cos^2\theta, \tag{4}$$

$$\Omega_{2\mathrm{c}j}^2 = \Omega_{2j}^2 - \omega_{\mathrm{c}j}^2, \tag{5}$$

where θ is the angle between $\vec{B}$ and $\vec{k}$, the respective plasma frequencies $\omega_{\mathrm{p}j} = q_j\sqrt{n_j/\epsilon_0 m_j}$, the thermal velocities $v_{T_j} = \sqrt{k_\mathrm{B}T_j/m_j}$, and the cyclotron frequencies $\omega_{\mathrm{c}j} = q_j B/m_j$. From the governing equations, the charge q_j, density n_j, mass m_j, neutral friction rate $\nu_{j\mathrm{n}}$, and drift velocity v_j are introduced. In the cold plasma limit this reduces to the formula in Ref. [27]. The susceptibility shows that the influence of the magnetic field is strongest for wave propagation perpendicular to the field, i.e., $\theta = \pi/2$. The unmagnetized limit is reached for $\theta = 0$ or

$$\omega_{\mathrm{c}j}^2 \ll (\omega_\mathrm{R} - \vec{k}\cdot\vec{v}_j)^2 - (\omega_\mathrm{I} + \nu_{j\mathrm{n}})^2, \tag{6}$$

where ω_R denotes the real and ω_I the imaginary part of ω. With the sample values introduced in Table II for the ions and using $\omega_\mathrm{R} \ll k v_\mathrm{i}$ as well as $\omega_\mathrm{I} \ll \nu_\mathrm{in}$, this condition is fulfilled by two to three orders of magnitude. In this case, $\Omega_{1\mathrm{ci}} \approx \Omega_{2\mathrm{ci}}$ cancels out from Eq. (1) and the ion susceptibility becomes independent of the magnetic induction. Therefore, in the present situation, the diagnostic of DDWs can be used in the same way as in the unmagnetized case [21].

The magnetic field influences the system only by magnetizing the electrons and therefore providing strong electron confinement perpendicular to the field lines. Additionally, the ion flow from the plasma to the wall shows an azimuthal component as the ions get deflected by the magnetic field. The azimuthal component of the ion flow can excite a rotation of the neutral gas and the dust cloud [29]. The tilt of the ion flow from the radial direction is roughly 14° at 100 mT and 4 Pa.

TABLE II. Parameters characterizing the magnetization of the plasma at 100 mT. These parameters comply with Eq. (6).

System frequencies	Symbol	Value
ion-cyclotron frequency	ω_ci	2.4×10^5 rad/s
ion-plasma frequency	ω_pi	$(2.1\text{–}6.6) \times 10^6$ rad/s
ion-neutral friction rate	ν_in	9.4×10^5 rad/s[a]
Doppler shift frequency	$k v_\mathrm{i}$	$(3.5\text{–}7) \times 10^6$ rad/s
Basic parameters	**Symbol**	**Value**
ion density	n_i	10^{14}–10^{15} m^{-3}
pressure	p	4 Pa
wave number	k	2–10 krad/m
ion drift velocity	v_i	1800–700 m/s

[a]Reference [28].

III. DUST-DENSITY WAVE DIAGNOSTIC

A. Method description

The dust-density wave diagnostic (DDW-D) is a method that relates the DDW frequency ω and wave number k to the plasma parameters ion density n_i and ion drift velocity v_i. Below, ω is always equivalent to ω_R from the preceding section. The method relies on the assumption that the fastest growing mode (k, ω) prevails at every location along the propagation direction of the wave. The quasineutrality condition is used to connect dust density n_d, ion density n_i, and dust charge q_d. For the dispersion relation of the DDW a hybrid ansatz is applied [30] using kinetic modeling of ions [31] and fluid modeling of dust and electrons [32]. Dust-neutral friction is modeled using the Epstein theory [33,34]. The value for the ion-neutral friction rate follows from the ion mobility measurements in Ref. [28].

Assumptions are an electron temperature of 5 eV, an ion and dust temperature of 25 meV, and a dust mass density of 1300 kg/m^3 [35]. The dust number density is attained by calibrating the intensity on the DDW camera with the optical depth measured on the photodiodes. The resulting density profiles from the center of the void along the radial direction are presented in Fig. 4.

A detailed explanation and application examples of the DDW-D can be found in Refs. [21,36]. A similar approach was used in different situations [37–39] to determine the dust charge.

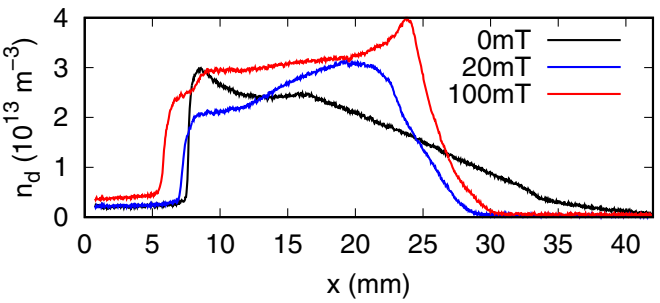

FIG. 4. Density distribution for the 0-, 20-, and 100-mT cases. The x axis is centered at the middle of the void. Within the void a nonzero density results from uncompensated multiple scattering. The total number of particles is not conserved but decreases. The sequence of measurements started with 100 mT and then the magnetic induction was reduced.

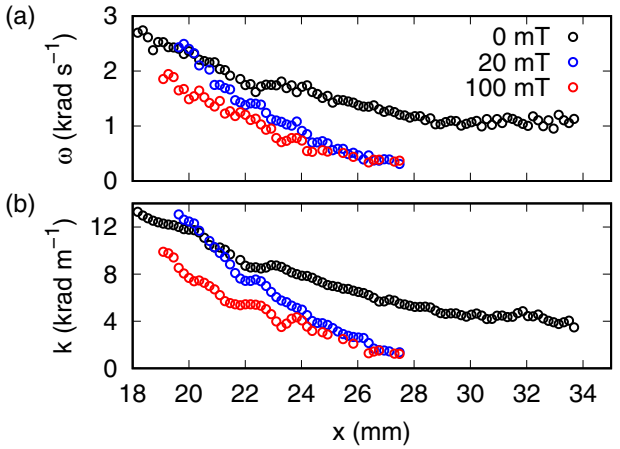

FIG. 5. (a) Wave frequency ω and (b) wave number k as calculated from the video data. The data are obtained from the central line of the FOV II. For both diagrams, the error of k and ω (standard deviation of the mean that follows from the frame-to-frame instantaneous values) is smaller than the diameter of the drawn circles.

B. Wave properties

The wave properties ω and k are extracted from a video with the help of the Hilbert transform [40]. A step-by-step scheme to calculate them from a video is given in Ref. [21].

In Fig. 5, ω and k are plotted along the radial direction at a central height between the electrodes. For this, a video from the FOV II (see Fig. 1) was taken with a frame rate of 2 kHz. Both ω and k have higher values in the unmagnetized case but show an almost identical development. They have high values in the center of the system and decrease towards the edge of the electrodes. In the magnetized cases, both k and ω approach zero between $x = 28$ and 30 mm. In the unmagnetized situation they remain at a constant level beyond $x = 30$ mm. The synchronous development of k and ω indicates that the wave propagates with constant phase velocity [21,36]. In Ref. [41] this is explained with the constant dust compressibility as an increase in the dust density is accompanied by a decrease in the dust charge.

C. Plasma parameters

With the application of the DDW-D, key parameters of a dusty plasma can be determined. In Fig. 6(a) the ion densities for the unmagnetized and the magnetized cases are compared. The ion density is in the same range in the unmagnetized and the magnetized cases and attains its maximum in the plasma center. In contrast to that, the dust density reaches its maximum around the void if no magnetic field is present or on a torus at the electrode edge with the presence of a magnetic field (see Fig. 4). We observe that the waves propagate from the center to the periphery of the system in all situations considered. This means that the ion flow is directed from the void to the wall and that the electric potential takes a maximum in the plasma center, i.e., the dust-density peak at the edge is not related to a potential maximum. The propagation direction can flip if the slope of the potential is inverted [42]. Additionally, the data show clearly that the ion density approaches zero at about $x = 30$ mm (100 mT) or spans widely into the volume (0 mT).

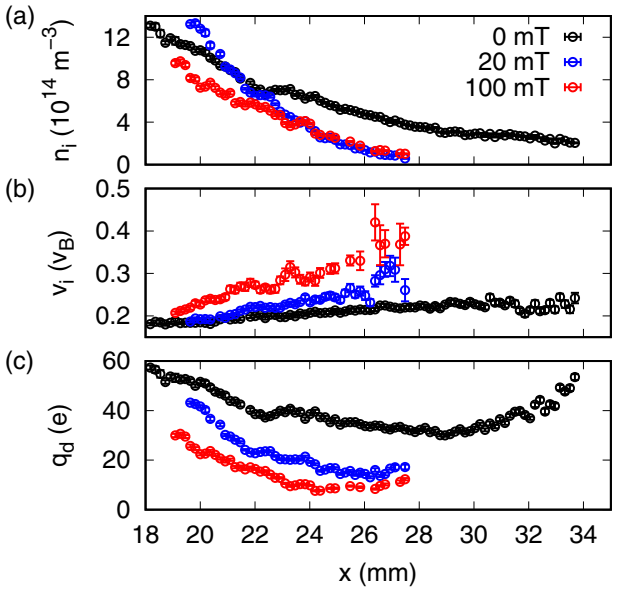

FIG. 6. (a) Ion density n_i, (b) ion drift velocity v_i as calculated from the DDW-D in units of the Bohm velocity $v_B = \sqrt{k_B T_e / m_i}$ with an estimated electron temperature of $T_e = 5$ eV, and (c) dust charge q_d. Error bars follow by error propagation of the errors in ω and k, which are described in the caption of Fig. 5.

A better understanding of the confinement situation can be expected from the analysis of the ion drift velocity v_i [Fig. 6(b)]. This velocity is directly connected to the electric field:

$$v_i = \mu(E)\, E. \tag{7}$$

The values of E can be calculated from v_i using the ion mobilities $\mu(E)$ provided in Ref. [28].

The ion drift velocity in the central part of the cloud is small as this is close to the symmetry center of the plasma, which has, by definition, no drift. In the position closest to the center, v_i is almost equal in all cases considered. Also, the drift velocity increases from the center to the edge of the plasma. Remarkably, the drift velocity increases much more strongly in the magnetized cases than in the unmagnetized case. For 100 mT it reaches twice the value of the unmagnetized case with a maximum of $0.47 v_B$. In terms of the electric field, this corresponds to about 1100 V/m, as can be found using Eq. (7). This is less than in a plasma sheath but much larger than in the bulk. The strong outward directed electric field explains why the negatively charged dust particles are confined in a cylindrical volume rather than filling the whole chamber. For comparison, in the unmagnetized case the maximum electric field is measured as 350 V/m. At an induction of 20 mT, the drift velocity is between the values reached for 0 and 100 mT. The same behavior of the ion drift was found using Langmuir probe measurements in the dust-free discharge but at higher neutral pressure and higher magnetic induction (see Figs. 6(c) and 6(f) in Ref. [20]).

Finally, the DDW-D provides the charge of the dust particles, shown in Fig. 6(c). Here q_d ranges between 31 and 57 elementary charges for 0 mT and between 8 and 32 for 100 mT, respectively. The difference can be attributed to the decaying

dust density while the magnetic inductions are set one after another. Due to a loss of particles between the measurements, the resulting charge on a single particle can be different in the presented cases. Nevertheless, they all show a decrease to a minimum and increase again towards the edge of the system.

The charge that a single dust particle with 150 nm in radius would obtain in an argon plasma with $T_e = 5$ eV and collisionless ions is about 1150 elementary charges, calculated from the charging currents of a spherical floating object [43]. The reduction to only some ten elementary charges is due to electron depletion in the plasma. This effect was first discussed for astrophysical situations [44,45], but electron depletion is also the main effect in the charging mechanism of dust particles in nanodusty plasmas.

IV. DUST-DENSITY DISTRIBUTION

A. Measurement method and data processing

For the measurement of the dust density, the telecentric lens is not protected with an interference filter. Instead, four images are taken to calculate the dust density: one image without any light source (dark image), one from the LED panel without dust and plasma (reference image), one with dust and plasma present but without LED light (plasma image), and one with dust, plasma, and LED lighting present (dust image). This yields the optical depth

$$\tau(x,z) = -\ln\left(\frac{\text{dust image} - \text{plasma image}}{\text{reference image} - \text{dark image}}\right). \quad (8)$$

Subtracting the plasma image from the dust image ensures that plasma glow does not contribute to the results. All images are averaged over 1 s (130 frames) to filter out noise and wave motion. Resulting images of the optical depth are shown in Fig. 7.

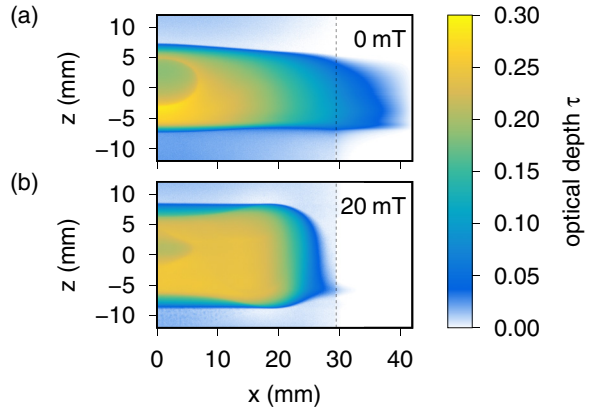

FIG. 7. Optical depth $\tau(x,z)$ as calculated with Eq. (8). (a) In the unmagnetized case, the cloud is weakly confined in the horizontal direction, leaping over the FOV of the telecentric lens. Therefore, the image is extrapolated using an exponentially decaying function beginning at the vertical dashed line. (b) With a magnetic field, the cloud is completely trapped within the FOV.

The dust density is calculated for the whole system using the inverse Abel transform on every line of sight:

$$\tau(x,z) = \int_{-\infty}^{\infty} \pi a^2 Q_{\text{ext}} n_d(x,y,z)\,dy, \quad (9)$$

$$n_d(r,z) = -\frac{1}{\pi^2 a^2 Q_{\text{ext}}} \int_r^{\infty} \frac{d\tau}{dx}(x,z) \frac{dx}{\sqrt{x^2 - r^2}}. \quad (10)$$

The variables x, y, and z correspond to coordinates given in Fig. 2, Q_{ext} denotes the extinction efficiency, n_d is the dust density, a is the dust particle radius, and r is the distance from the central axis of the experiment. The infinite limits in the integrals of Eqs. (9) and (10) disappear when regarding a finite density distribution.

B. Resulting distributions

The extinction measurement provides an image of the dust cloud with the cloud appearing as a shadow in front of the bright LED panel as in Fig. 7. As Eqs. (9) and (10) include the extinction efficiency Q_{ext} and the particle radius a, extinction images only allow one to calculate n_d with information about the particle properties which are provided here using the CRAS-Mie algorithm [23]. Since our system is losing particles that leak out of the confinement, the total number of dust particles is not constant over time. With the 2D density information obtained in Figs. 8(a)–8(e), the total number of particles is calculated. As can be seen from Fig. 8, this number starts at about 3.0×10^9 [Fig. 8(a)] and then drops down to 1.4×10^9 [Fig. 8(e)].

The resulting density distribution shows multiple features. At the highest magnetic induction [Fig. 8(a)], the density is peaked at the periphery of the system at roughly $x = 24$ mm, which practically coincides with the electrode edge at $x = 25$ mm. From this peak the density drops rapidly in the outward direction, while it drops gradually towards the center. The DDW-D results show that the latter can be attributed to the strong electric confinement of the cloud and plasma in the magnetized case. In the center, there still is a void indicating an ion density maximum resulting in an ion flow directed away from the center. Surprisingly, the dust density within the cloud has a minimum around the void, which is in complete contrast with the unmagnetized situation, where a density maximum surrounds the void as shown in Figs. 8(e) and 4.

The density maximum at the void edge is the commonly observed unmagnetized configuration [26,46,47]. When the magnetic induction is decreased as in Figs. 8(b)–8(d), the density peak gets broader and moves towards the center. Finally, the distribution is peaked around the void at 0 mT, visible in Fig. 8(e).

V. DISCUSSION

As the dust charge and the dust density are known, one can make an estimate of the forces that keep the dust particles in place. Since the system is in equilibrium, the confining forces $q_d E$ are compensated by the gradient of the electrostatic pressure and the ion drag.

With a magnetic field, the density peak from the void edge gets shifted to the periphery of the cloud. As derived from the DDW-D, the plasma only generates a stronger confining

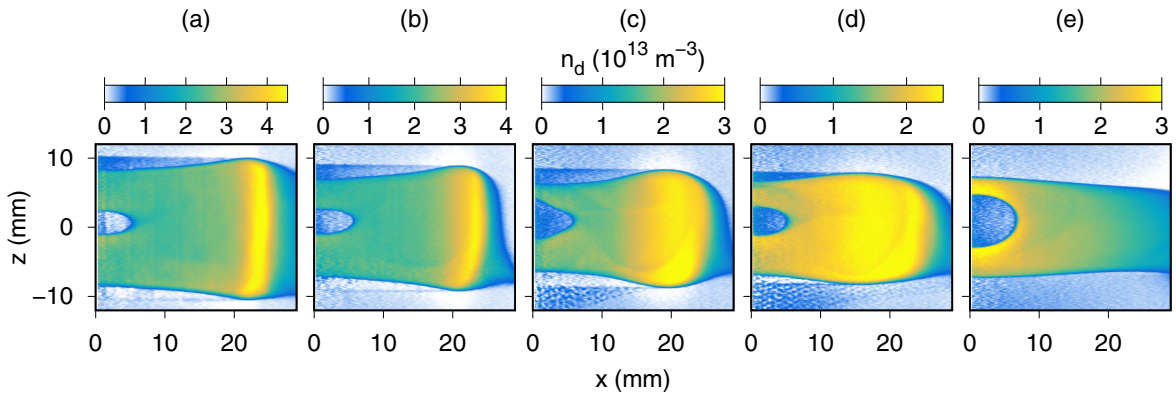

FIG. 8. Dust density as calculated with Eq. (10). The color axis is adjusted from (a) to (e) as the total number of particles N decreases: (a) $N = 3.0 \times 10^9$ with $B = 100$ mT, (b) $N = 1.9 \times 10^9$ with $B = 50$ mT, (c) $N = 1.6 \times 10^9$ with $B = 20$ mT, (d) $N = 1.6 \times 10^9$ with $B = 10$ mT, and (e) $N = 1.4 \times 10^9$ with $B = 0$ mT.

electric force but does not change its center-peaked density and potential distribution. If there is no additional force, this should still yield the dust-density maximum at the void edge.

To resolve this contradiction, we propose a rotation of the dust cloud. A centrifugal force would explain the shift of the density peak. Such a rotation can be driven by the ion drag. With the presence of the magnetic field, ions get deflected from the radial into the azimuthal direction and thus transfer momentum in the azimuthal direction on the dust particles. In our case, the immediate ion drag force [48] is weak as the charge of the particles is low. However, earlier studies showed that in many cases the cause of rotating dust in magnetized plasmas is a neutral drag because the ion flow sets the working gas into rotation [29] by ion-neutral collisions. The neutral flow is only weakly damped by viscosity.

From Fig. 6(c) one can find that the dust particles in the density peak carry roughly ten elementary charges at 100 mT. Here the DDW-D provides an electric field of 450 V/m. The electrostatic force for such particles equals $F_E \approx 7 \times 10^{-16}$ N. Assuming a centrifugal force that amounts to at least 10% of the confining force to significantly influence the spatial distribution, a rotation frequency

$$f \approx \sqrt{\frac{0.1 F_E}{4\pi^2 m_d r}} \approx 2 \text{ Hz} \tag{11}$$

can be calculated which is not more than an order of magnitude estimate. In Ref. [49] a nanoparticle cloud rotation in a system with magnetic inductions about 1 mT was also conjectured from the observation of a rotating plasma glow profile. In our setup, the particle movement inside a complex nanodusty fluid is inaccessible. Different experimental approaches for this kind of problem are needed in future works on this subject. Laser Doppler anemometry is a method to resolve particle flows inside the system. It has been applied to an unmagnetized dusty plasma in Ref. [50].

VI. SUMMARY

In this paper we have shown diagnostic results of a dust cloud confined in a magnetized plasma. The data show that the confinement situation can be significantly influenced by the magnetic field that provides strong confinement of the electrons and hence also of the dust cloud perpendicular to the field lines. From the analysis of DDWs it was found that the electric field at the electrode edge in such a system is more than 1000 V/m, which is almost comparable to the sheath of the plasma.

Additionally, from the spatially resolved density provided from Abel-inverted extinction images of the dust cloud, one can find that the density profile of dust particles changes its distribution when a magnetic field is applied. The first effect is due to the strong confinement at the electrode edge, which leads to a very steep density gradient there. A second effect appears within the dust cloud: The density distribution shifts from being peaked around the void to peaked in front of the electrode edge resembling a hollow profile. In our experimental study this shift was gradual from being strong at high magnetic inductions to weak at low magnetic inductions. The void phenomenon itself remains almost unchanged, which confirms that the ion density remains center peaked. As we observe that DDWs propagate from the center to the periphery, it can be inferred that also the plasma potential remains center peaked even in the magnetized situation. With the data provided from our DDW-D method, we propose that the density shift is caused by a rotation of the dust cloud while a magnetic field is present.

ACKNOWLEDGMENTS

Technical support from M. Knüppel, M. Poser, and V. Rohwer is gratefully acknowledged. We thank O. Asnaz for debugging the DDW-D code and N. Rehbehn for carefully programming the laboratory software. This work was supported by the Deutsche Forschungsgemeinschaft DFG in the framework of the SFB-TR24 Greifswald-Kiel, Project A2.

[1] E. Thomas, Jr., R. L. Merlino, and M. Rosenberg, Plasma Phys. Controlled Fusion **54**, 124034 (2012).
[2] J. Winter, Phys. Plasmas **7**, 3862 (2000).
[3] J. Winter, Plasma Phys. Controlled Fusion **46**, B583 (2004).
[4] D. A. Mendis, Plasma Sources Sci. Technol. **11**, A219 (2002).
[5] D. L. Rudakov *et al.*, Rev. Sci. Instrum. **79**, 10F303 (2008).
[6] S. I. Krasheninnikov, R. D. Smirnov, and D. L. Rudakov, Plasma Phys. Controlled Fusion **53**, 083001 (2011).
[7] V. N. Tsytovich, N. Sato, and G. E. Morfill, New J. Phys. **5**, 43 (2003).
[8] D. Lange, J. Plasma Phys. **82**, 905820101 (2016).
[9] T. Ott and M. Bonitz, Phys. Rev. Lett. **107**, 135003 (2011).
[10] T. Ott, H. Löwen, and M. Bonitz, Phys. Rev. Lett. **111**, 065001 (2013).
[11] J. Carstensen, F. Greiner, and A. Piel, Phys. Rev. Lett. **109**, 135001 (2012).
[12] J.-P. Joost, P. Ludwig, H. Kählert, C. Arran, and M. Bonitz, Plasma Phys. Controlled Fusion **57**, 025004 (2015).
[13] H. Kählert, J. Carstensen, M. Bonitz, H. Löwen, F. Greiner, and A. Piel, Phys. Rev. Lett. **109**, 155003 (2012).
[14] M. Rosenberg, Phys. Scr. **89**, 085601 (2014).
[15] Y. Saitou and O. Ishihara, Phys. Rev. Lett. **111**, 185003 (2013).
[16] S. Knist, F. Greiner, F. Biss, and A. Piel, Contrib. Plasma Phys. **51**, 769 (2011).
[17] E. Thomas, U. Konopka, D. Artis, B. Lynch, S. Leblanc, S. Adams, R. L. Merlino, and M. Rosenberg, J. Plasma Phys. **81**, 345810206 (2015).
[18] M. Schwabe, U. Konopka, P. Bandyopadhyay, and G. E. Morfill, Phys. Rev. Lett. **106**, 215004 (2011).
[19] E. Thomas, Jr., U. Konopka, R. L. Merlino, and M. Rosenberg, Phys. Plasmas **23**, 055701 (2016).
[20] B. Tadsen, F. Greiner, and A. Piel, Phys. Plasmas **21**, 103704 (2014).
[21] B. Tadsen, F. Greiner, S. Groth, and A. Piel, Phys. Plasmas **22**, 113701 (2015).
[22] F. Greiner, J. Carstensen, N. Köhler, I. Pilch, H. Ketelsen, S. Knist, and A. Piel, Plasma Sources Sci. Technol. **21**, 065005 (2012).
[23] S. Groth, F. Greiner, B. Tadsen, and A. Piel, J. Phys. D **48**, 465203 (2015).
[24] F. Kirchschlager, S. Wolf, F. Greiner, S. Groth, and A. Labdon, Appl. Phys. Lett. **110**, 173106 (2017).
[25] C. Killer, F. Greiner, S. Groth, B. Tadsen, and A. Melzer, Plasma Sources Sci. Technol. **25**, 055004 (2016).
[26] C. Killer, M. Himpel, and A. Melzer, Rev. Sci. Instrum. **85**, 103711 (2014).
[27] Compare Eq. (1) in P. Bezbaruah and N. Das, Phys. Plasmas **23**, 043701 (2016).
[28] L. S. Frost, Phys. Rev. **105**, 354 (1957).
[29] J. Carstensen, F. Greiner, L.-J. Hou, H. Maurer, and A. Piel, Phys. Plasmas **16**, 013702 (2009).
[30] W. D. S. Ruhunusiri and J. Goree, Phys. Plasmas **21**, 053702 (2014).
[31] M. Rosenberg, J. Vac. Sci. Technol. A **14**, 631 (1996).
[32] N. Rao, P. Shukla, and M. Yu, Planet. Space Sci. **38**, 543 (1990).
[33] J. Carstensen, F. Haase, H. Jung, B. Tadsen, S. Groth, F. Greiner, and A. Piel, IEEE Trans. Plasma Sci. **41**, 764 (2013).
[34] P. S. Epstein, Phys. Rev. **23**, 710 (1924).
[35] A. C. Ferrari, A. Libassi, B. K. Tanner, V. Stolojan, J. Yuan, L. M. Brown, S. E. Rodil, B. Kleinsorge, and J. Robertson, Phys. Rev. B **62**, 11089 (2000).
[36] B. Tadsen, F. Greiner, and A. Piel, Phys. Plasmas **24**, 033704 (2017).
[37] V. E. Fortov, A. G. Khrapak, S. A. Khrapak, V. I. Molotkov, A. P. Nefedov, O. F. Petrov, and V. M. Torchinsky, Phys. Plasmas **7**, 1374 (2000).
[38] S. Ratynskaia, S. Khrapak, A. Zobnin, M. H. Thoma, M. Kretschmer, A. Usachev, V. Yaroshenko, R. A. Quinn, G. E. Morfill, O. Petrov, and V. Fortov, Phys. Rev. Lett. **93**, 085001 (2004).
[39] S. Ratynskaia, M. Kretschmer, S. Khrapak, R. Quinn, M. Thoma, G. Morfill, A. Zobnin, A. Usachev, O. Petrov, and V. Fortov, IEEE Trans. Plasma Sci. **32**, 613 (2004).
[40] K. O. Menzel, O. Arp, and A. Piel, Phys. Rev. E **83**, 016402 (2011).
[41] D. I. Zhukhovitskii, Phys. Rev. E **92**, 023108 (2015).
[42] C. Schmidt, O. Arp, and A. Piel, Phys. Plasmas **18**, 013704 (2011).
[43] H. M. Mott-Smith and I. Langmuir, Phys. Rev. **28**, 727 (1926).
[44] C. K. Goertz and W.-H. Ip, Geophys. Res. Lett. **11**, 349 (1984).
[45] O. Havnes, G. E. Morfill, and C. K. Goertz, J. Geophys. Res. **89**, 10999 (1984).
[46] H. Rothermel, T. Hagl, G. E. Morfill, M. H. Thoma, and H. M. Thomas, Phys. Rev. Lett. **89**, 175001 (2002).
[47] V. N. Naumkin, D. I. Zhukhovitskii, V. I. Molotkov, A. M. Lipaev, V. E. Fortov, H. M. Thomas, P. Huber, and G. E. Morfill, Phys. Rev. E **94**, 033204 (2016).
[48] M. S. Barnes, J. H. Keller, J. C. Forster, J. A. O'Neill, and D. K. Coultas, Phys. Rev. Lett. **68**, 313 (1992).
[49] M. Schulze, D. O'Connell, T. Gans, P. Awakowicz, and A. von Keudell, Plasma Sources Sci. Technol. **16**, 774 (2007).
[50] See Sec. 3.1 in A. Bouchoule and L. Boufendi, Plasma Sources Sci. Technol. **2**, 204 (1993).